Electronic Supplementary Material (ESI) for Materials Horizons.

Supporting Information

Scalable Nanoporous Carbon Films Allow Line-of-Sight 3D Atomic Layer Deposition of Pt: Towards a New Generation Catalyst Layer for PEM Fuel Cells

Marwa Atwa,[a,g] Xiaoan Li,[a,h] Zhaoxuan Wang,[b] Samuel Dull,[c] Shicheng Xu,[d] Xia Tong,[a] Rui Tang,[e] Hirotomo Nishihara,[e] Fritz Prinz,[b,d,f] and Viola Birss*[a]

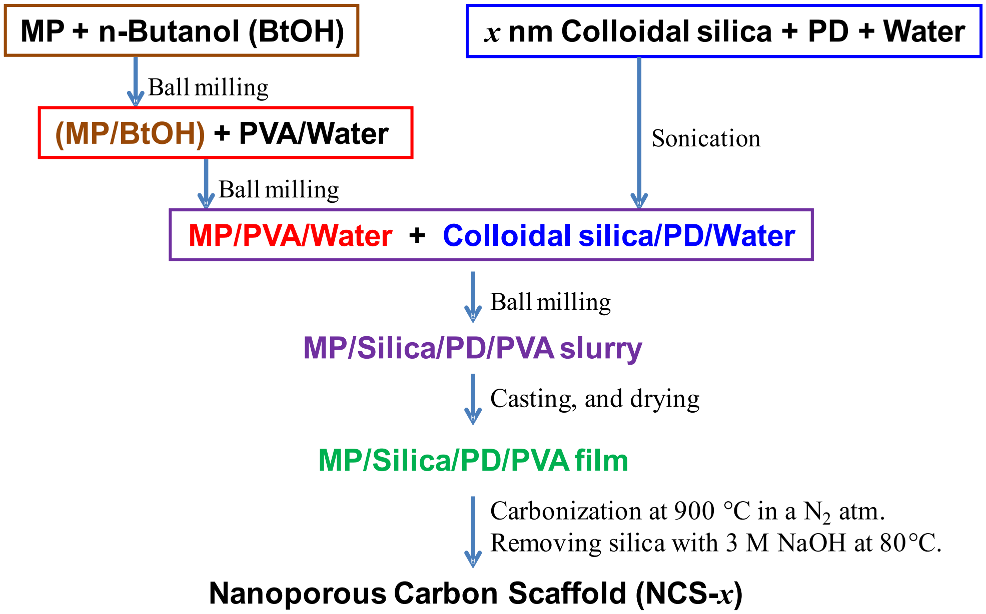

Fig. S1. Flow chart showing the fabrication of the nanoporous carbon scaffold (NCS), where MP = mesophase pitch, PVA = poly(vinyl alcohol), PD = 1,3-propanediol, and x is the particle size of colloidal silica in nanometers.

Table S1. Comparison of synthesis method and structural properties of self-supported (binder-free) nanoporous carbon films in the literature

Deposition method	Maximum sheet area [cm^2]	Scalable	Thickness [μm]	Pore dia [nm]/ Monodisperse?	Fully Tunable Pore Size	3-D Connected Pores	Surface area [m^2/g]	Pore volume [cm^3/g]	Ref.
NCS (tape-casting)	1 - 130+	YES	1 - 100	5 - 100+/ YES	YES	YES	200 - 600	1.2 - 2.6	This work[8]
Doctor blade casting	15 × 100 = 1500	YES	30 - 50	NDA[a] /NDA[b]	NO	NO	200 - 500	NDA[b]	6
Doctor blade casting	NDA[b]	YES	5 - 300	50[c]- 5000 /NO	NO	NO[d]	NDA[b]	NDA[b]	7
Filtration, thermal reduction	NDA[b]	NO	2.65	18 – 56/ NO	YES	NO	36	NDA[b]	5
Doctor blade casting	~ 1.5	NO	18 - 42	~ 6/ YES	NO	NO[d]	335 - 430	0.36 - 0.46	48
Spin-coating	2 × 2 = 4	NO	0.09 - 3	~ 4.3/ YES	YES	YES	700	0.46	49
Chemical vapor deposition	0.4 × 0.9 = 0.36	NO	200	5 – 7/ YES	NO	YES	1500	3.2	50
Dropwise and then evaporation	0.25	NO	30 - 150	8/ YES	NO	YES	746	NDA[b]	18, 51
Nano-casting	0.8 × 0.6 = 0.48	NO	-2000	2.8, 286/ NO	NO	YES	1261	0.93	52
Spin-coating, etch	~ 4	NO	0.45	~ 4/ YES	NO	YES	2030	NDA[b]	53

[a] Pore sizes not reported but surface area range implies mesoporous structure.

[b] NDA = No Data Available

[c] Contains large pores, mostly out of mesoporous range

[d] Primarily 2-D interconnected pores across membrane

EXPERIMENTAL RESULTS

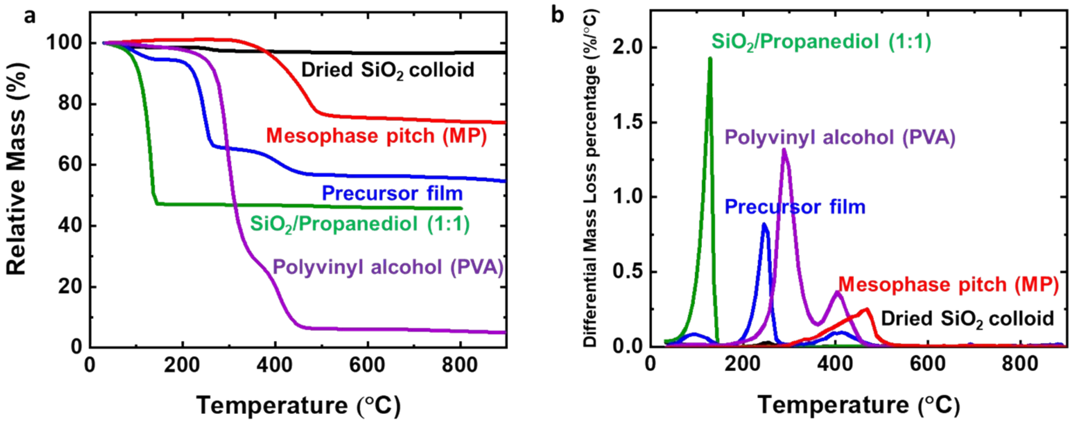

Fig. S2. (a) Thermogravimetric and (b) differential thermogravimetric profiles of as-cast precursor film (blue), dried silica colloid (black), mesophase pitch (MP, red), polyvinyl alcohol (PVA, violet), and a silica/1,3-propanediol mixture (green) in a N_2 flow at a heating rate of 2 °C/min.

When heated to 500 °C, the PVA-derived low-aromatic pitch decomposes or volatizes, leaving only ~5% of its original mass in the form of carbon, as shown by thermogravimetric analysis (TGA) (Fig. S2/S3). The PVA-derived pitch may also be imprinted by the silica template, along with the MP. The thermal decomposition of the precursor film (mixture of MP, SiO_2, PD and PVA) at 250-350 °C produces only water, acetic acid and acetaldehyde, as determined by mass spectrometry (Fig. S4), with the remainder being just carbon and the silica template, as desired.

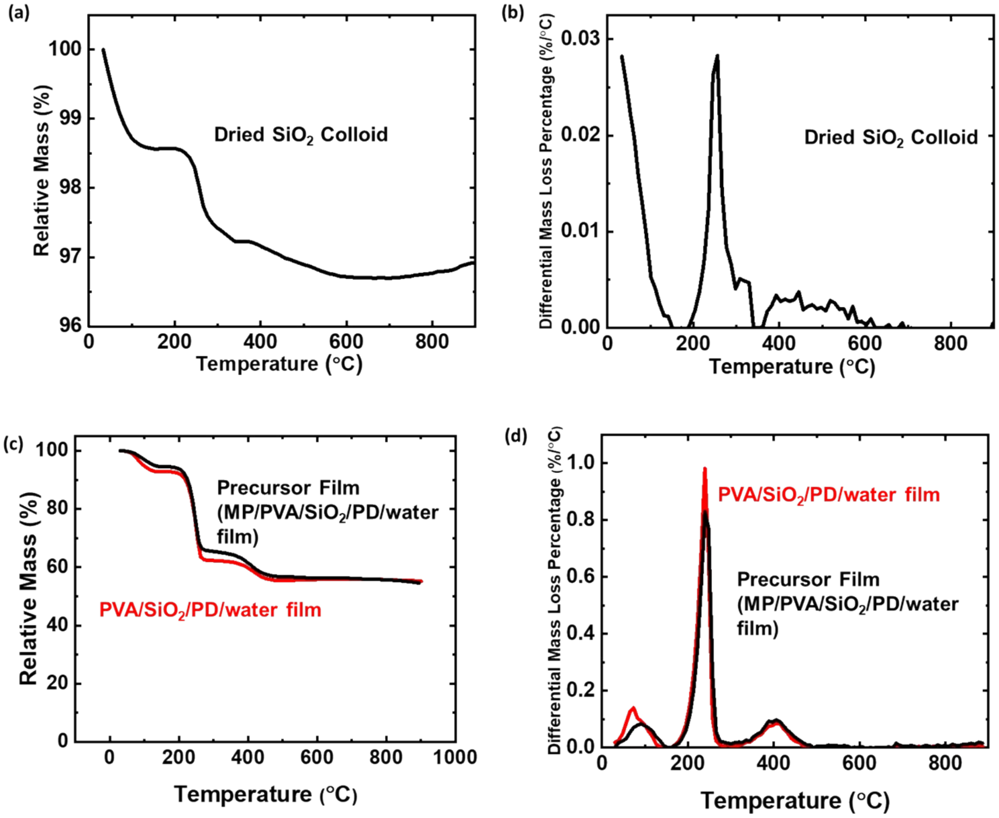

Fig. S3. (a,c) Thermogravimetric and (b,d) differential thermogravimetric profiles of (a,b) silica colloid, dried under room conditions overnight before testing and (c,d) a PVA/silica/PD film and the precursor film, all in a N_2 flow at a heating rate of 2 °C.min^{-1}.

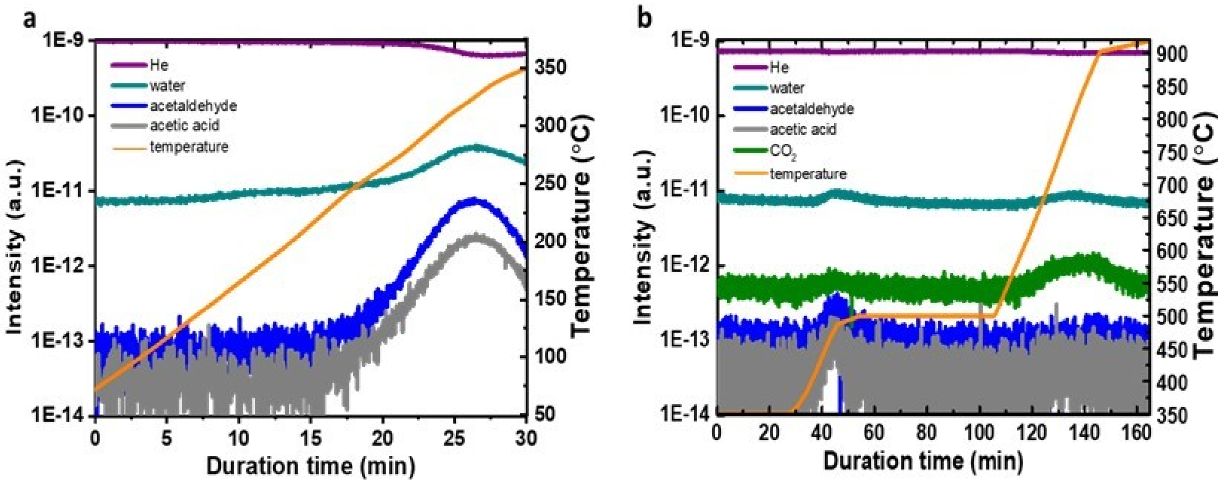

Fig. S4. Mass spectrometry analysis of gas evolution during heating of the NCS precursor films from (a) 50 °C to 350 °C and (b) 350 °C to 900 °C.

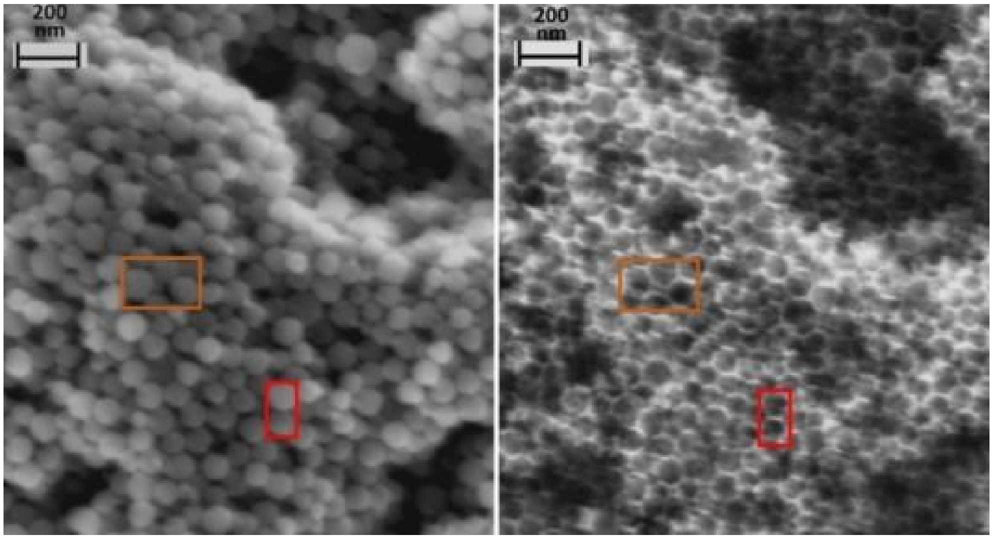

Fig. S5. FESEM images of the identical location within a piece of NCS85 (a) before and (b) after the removal of the silica nanoparticles. This demonstrates that the silica colloids are responsible for the formation of the pores within the final NCS product, while also showing the advantages of a sheet material (NCS) in terms of imaging precisely the same location before and after various processing and/or testing steps.

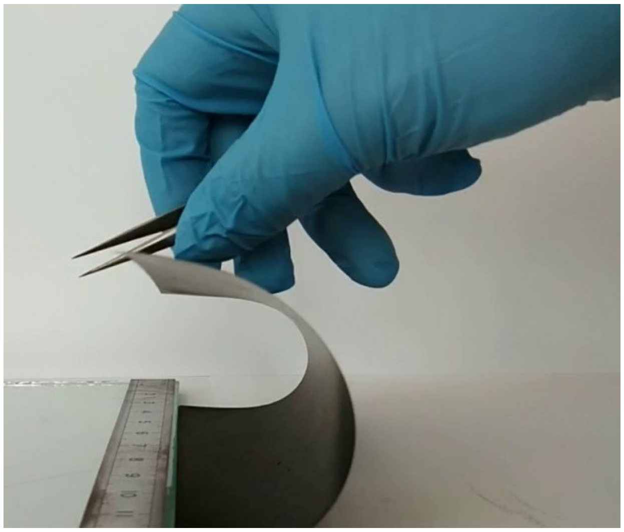

Fig. S6. Photograph of NCS in the final stage of preparation after silica removal, showing its elastic properties, also demonstrated in Video S2.

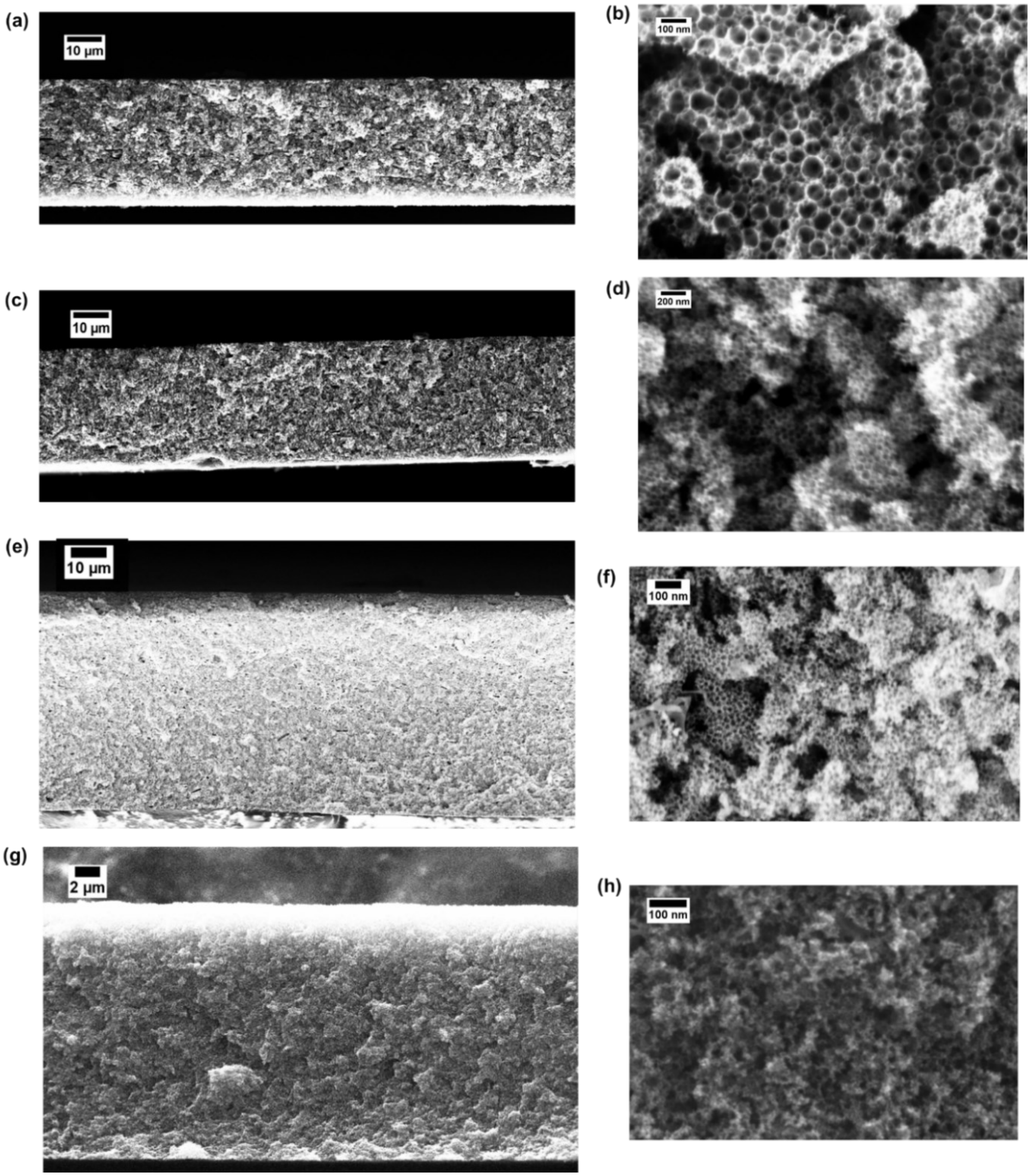

Fig. S7. Cross-sectional FESEM images of (a,b) NCS85, (c,d) NCS50, (e,f) NCS22 and (g,h) NCS8 films where (a,c,e,g) are low magnification and (b,d,f,h) are high magnification images.

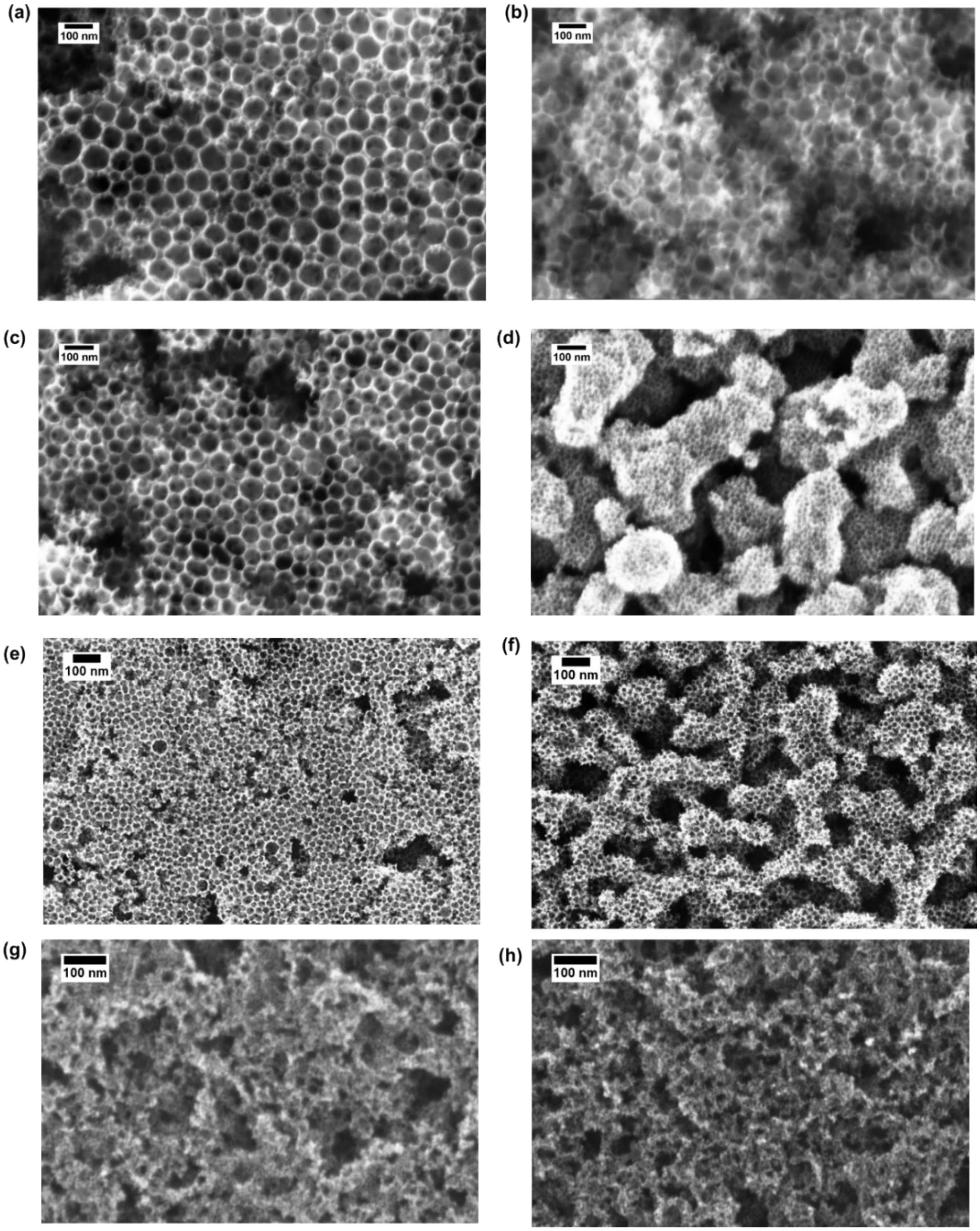

Fig. S8. FESEM images of NCS85, NCS50, NCS22 and NCS8 films, respectively, where (a, c, e and g) show the glass-side of the before-mentioned films respectively while (b, d, f and h) show the air-side.

The two sides of the NCS membranes (Fig. S8) have slightly different properties, with the glass side (lower, L-side) being a bit smoother at the macroscopic scale than the air side (upper, U-side). The glass side is a bit smoother (Fig. S8), advantageous for imaging purposes, while the slightly rougher air side would make a better bond to a second material. However, the roughness does not fully penetrate into the NCS.

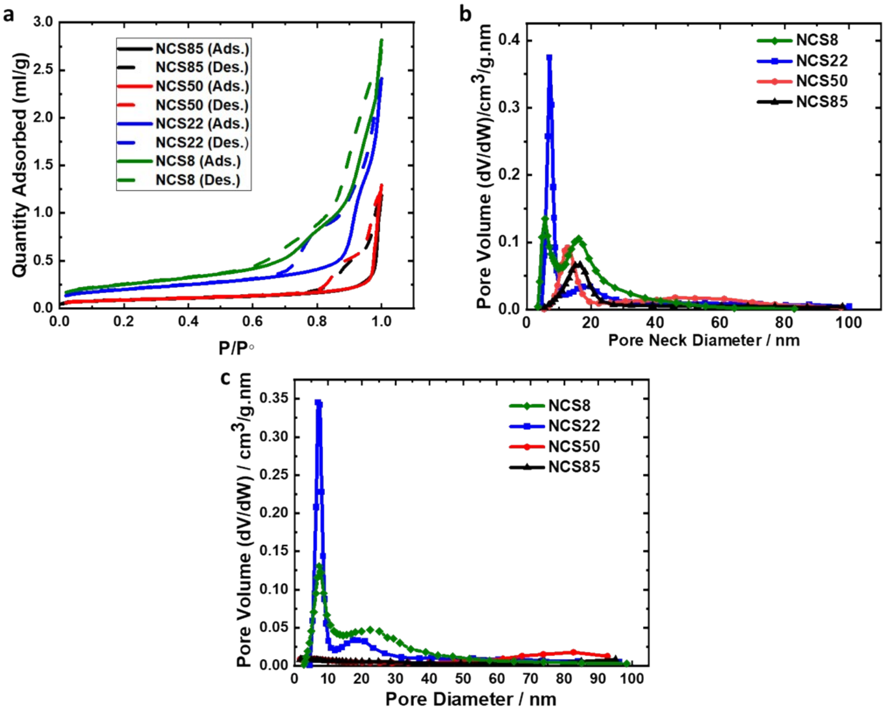

Fig. S9. (a) N_2 adsorption (solid line) and desorption (dashed line) data for the nanoporous carbon scaffolds with different pore sizes. (b and c) show the corresponding pore size distributions of the NCS materials, calculated from the (b) desorption and (c) adsorption branches of the isotherm using the Barrett-Joyner-Halenda (BJH) method, with the *t*-curve of carbon black used as the standard to determine the statistical thickness of the adsorbed nitrogen film.

The N_2 gas sorption isotherms of NCS films with different pore sizes and the corresponding distribution of the NCS pore sizes and pore neck diameters are shown in Fig. S9, with the data summarized in Table S2. N_2 sorption isotherms (NSI) of the NCS materials were obtained in order to determine their internal pore structure (Fig. S9a). The Barrett-Joyner-Halenda (BJH) method was used to analyze the N_2 adsorption and desorption branches of the isotherms of the NCS films (Figs.

S9b and S9c).[51] The microporosity of the NCS films is 20 % or lower (Table S2), similar to what was seen for silica colloid-imprinted carbon powders, made using similar methods.[55]

Notably, the pore size distribution (PSD) of NCS50 and NCS85, obtained from the adsorption branch, is likely not that useful, as BJH analysis of gas sorption data is not reliable for materials with large pore sizes (≥ 50 nm). Therefore, the PSD of the NCS-50 and NCS85 materials was obtained from SEM images, as shown in Fig. 2c and b.

According to an IUPAC Technical Report in 2015,[56] the hysteresis in the nitrogen sorption data for the NCS films is Type H2(b) (Fig. S9a), which indicates the presence of pore necks (Figs. 2e and Fig. S9b) between neighboring pores. The necks are a natural outcome of the filling of the pores between close packed spherical silica particles in the dried precursor film during the imprinting stage, as shown in the schematic of Fig. 1b. The MP particles will soften, with the pitch diffusing between the silica nanoparticles, producing pore necks.

Sample	Pore Size [nm][a]	Neck Size [nm][b]	S_{BET} [m^2/g][c]	$S_{external}$ [m^2/g][d]	S_{micro} [m^2/g][e]	S_{micro}/S_{BET} [%]	V_{NSI} [ml/g][f]	V_{micro} [ml/g][d]	V_{micro}/V_{NSI}
NCS85	82±12	16±1	194±5	162±1.4	32±3.4	16.2	1.2 ±0.1	1.6E-02	1.32
NCS50	46±5	12.0 ± 0.3	280±20	221±17.7	59±1.4	22.5	1.8±0.1	3.0E-02	1.60
NCS22	22±2	7.0 ± 0.4	483±5	412±1.6	71±3.7	14.7	2.2±0.0	3.5E-02	1.59
NCS8	7.4±0.1	5.7±0.1	575±5	524±0.5	51±0.5	8.9	2.6±0.1	2.4E-02	0.92

Table S2. Structural properties of NCS materials of varying pore size

[a] Pore size obtained from the maximum in the pore size distribution plots (gas sorption) in Fig. S9c for NCS22 and NCS8, while pore size of NCS85 and NCS50 are obtained by averaging the width of more than 100 pores in the FESEM images in Fig. 2b and 2c.

[b] Pore neck width obtained from the maximum in the pore size distribution plots in Fig. S9b.

[c] S_{BET} = total surface area, obtained using the Brunauer-Emmett-Teller (BET) plot in the partial pressure range of $0.05 < P/P_o < 0.30$.

[d] $S_{external}$ = external surface area and V_{micro} = micropore volume, both obtained using the *t*-plot method in the partial pressure range of $0.2 < P/P_o < 0.5$, with carbon black used as the reference.

[e] S_{micro} = micropore surface area, obtained by subtracting the external surface area ($S_{external}$) from the total surface area (S_{BET}).

[f] V_{NSI} = pore volume, acquired from N_2 adsorption isotherms at $P/P_o = 0.98$.

Table S3. Porosity measurements of NCS using helium pycnometry

Sample	Bulk Density [g/cm^3][a]	Grain Density [g/cm^3][b]	Ɛ, porosity [%][c]
NCS85	0.27	2.1	87
NCS50	0.22	1.9	88
NCS22	0.24	2.0	88

[a] Bulk density calculated from measured mass of 10 cm^2 NCS film with a 35 µm thickness.

[b] Grain density obtained experimentally using He pycnometry.

[c] Porosity calculated using bulk and grain density of NCS as follows: Porosity=1 - (bulk density/grain density) × 100%.

Electrochemical and Surface Properties of NCS

The total gravimetric capacitance values (double layer capacitance + pseudocapacitance), obtained from the CVs in Fig. 3a at 10 mV/s, are given in Table S4, where the average capacitance was obtained by integrating the full charge passed in a potential scan between 0.05 and 1.1 V vs. RHE and dividing by the potential range scanned (1.05 V), given per weight of NCS used in each experiment. Approximately one sixth of the total capacitance comes from the pseudocapacitance, which reflects the functional group density of the carbons, i.e., the higher the ratio, the higher the surface oxygen group density.

The NCS materials examined herein all have a similar functional group surface density, but these are much larger than conventional carbon blacks such as Vulcan Carbon (VC, which has almost no surface functional groups on its surface).[57] This high surface functional group density of the NCS is related to the hard-template synthesis approach used here, based on our parallel results with other hard-templated carbons.[58] Notably, the larger the surface area (the smaller the pore size), the higher the total oxygen functional groups content per gram of NCS (Table S4). The TPD results (Fig. S15, Table S4) also show that this correlates with a higher total number of H-terminated edge sites.

The favorable electrochemical and surface properties of our NCS membranes is a direct result of the combination of low tortuosity, high porosity (90%), and its fully 3D interconnected porous structure. Further, the NCS has a high edge site density, making it very wettable, Fig. S14. To the best of our knowledge, these combined beneficial characteristics are a major advancement compared to all previously reported carbon films.

Table S4: Summary of pseudocapacitance and surface oxygen concentration of three NCS materials as a function of pore size, determined using cyclic voltammetry (CV) and temperature programmed desorption (TPD).

Sample	Specific pseudo-capacitance [F/g]^a	Specific DL Capacitance [F/g]^b	Pesudo-capacitance contribution to total capacitance [%]^c	ECSA [m^2/g]^d	Oxygen content from CO [μmol/g]^e	Oxygen content from CO_2 [μmol/g]^f	Total oxygen content ($2CO_2$+CO) [μmol/g]	H-terminated active sites [μmol/g]^g
NCS85	3.7	25.7	12.6	196	479	89	557	2230
NCS50	5.3	37.4	12.4	285	769	187	1140	2150
NCS22	11.0	59.8	15.5	472	1030	207	1440	2630

[a] Obtained by integrating the CV charge in the redox peaks between 0.25 and 0.80 V (vs. RHE) and dividing the charge by the potential difference of 0.7 V.

[b] Obtained by subtracting the pseudo-capacitance charge from the total gravimetric charge and then dividing this value by the potential difference of 1.05 V.

[c] Obtained by dividing specific pseudocapacitance by total double layer (DL)capacitance.

[d] Obtained by dividing the total capacitance (double layer and pseudocapacitance in F/g) by 0.15 F.m^{-2}.

[e] Obtained by integrating the area under the CO broad peak in TPD pattern, Fig. S15.

[f] Obtained by integrating the area under the CO_2 broad peak in TPD pattern, Fig. S15.

[g] Obtained by integrating the area under the H_2 peak in TPD pattern, Fig. S16.

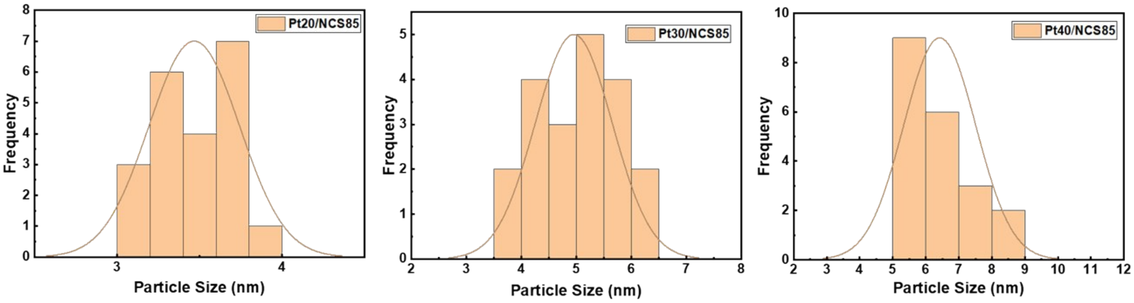

Fig. S10. Pt NP size distribution of the Ptx/NCS85 samples, calculated from the TEM analysis of approximately 30 NPs (Fig. 4a-c).

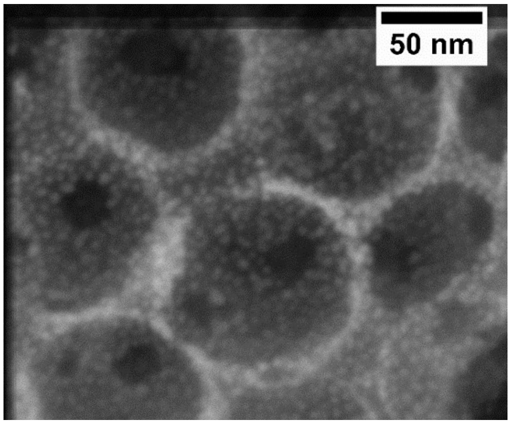

Fig. S11. FESEM image of one region of Pt20/NCS85, showing Pt NP distribution and size.

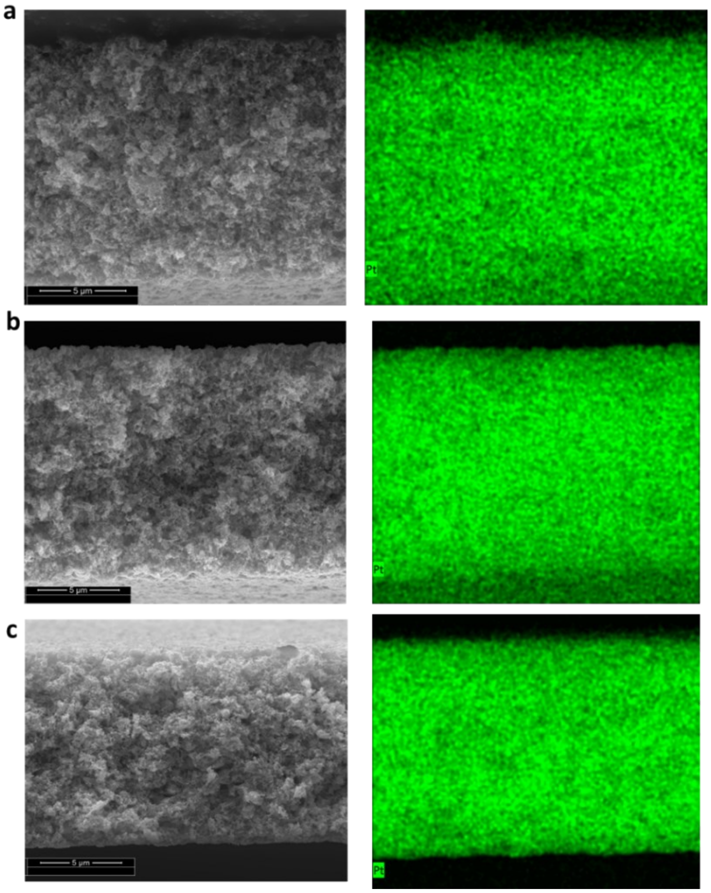

Fig. S12. EDX mapping of Pt of the full cross section of the Pt/NCS85 samples. (a) Pt20/NCS85, (b) Pt30/NCS85 and (c) Pt40/NCS85.

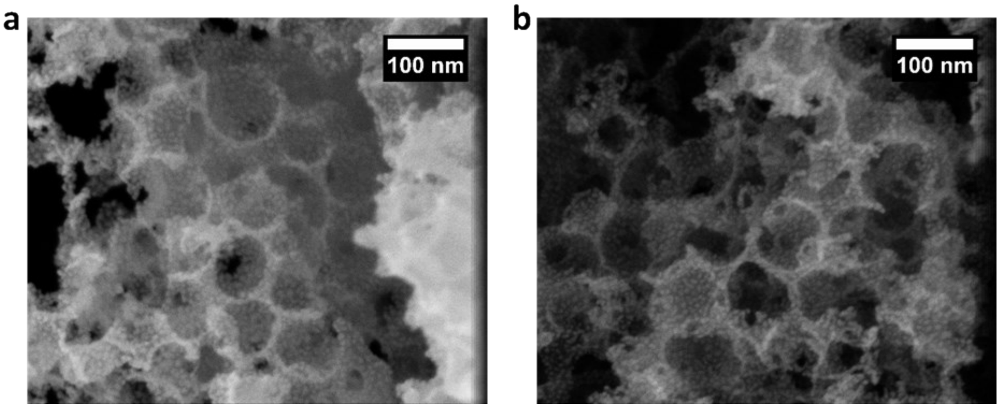

Fig. S13. FESEM images of the cross-section of Pt30/NCS85, showing a region (a) near the front face of the NCS sheet and (b) near the back.

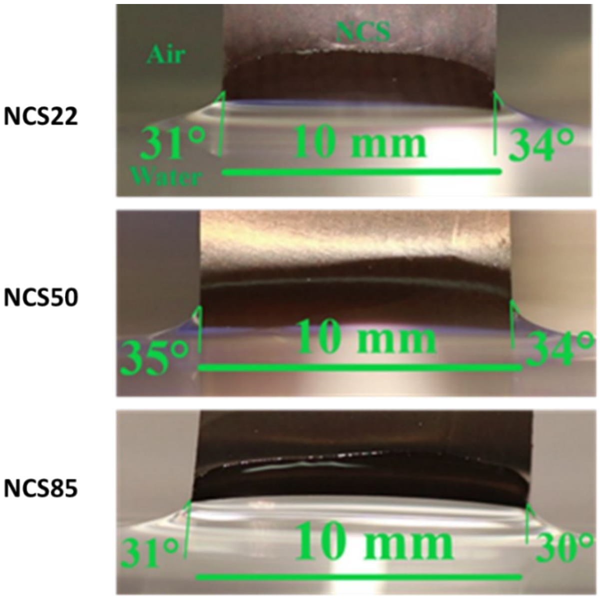

Fig. S14. Contact angle measurements of NCS with different pore sizes.

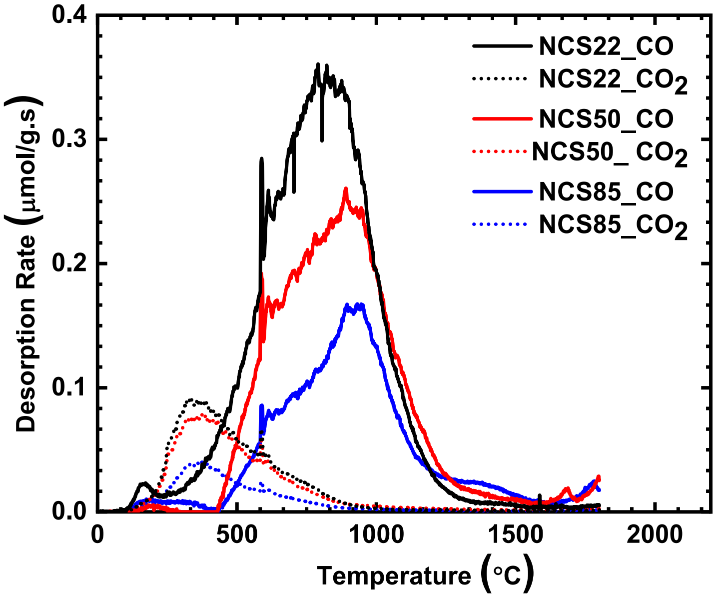

Fig. S15. CO and CO_2 production at NCS85, NCS50 and NCS22 during TPD measurements.

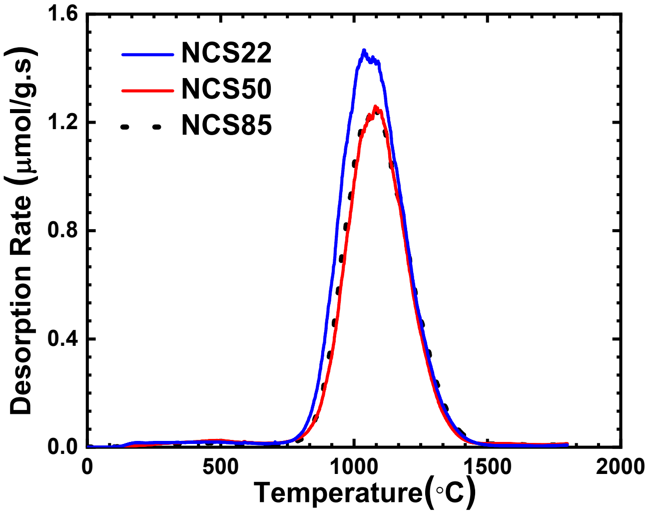

Fig. S16. H_2 production at NCS85, NCS50 and NC22 during TPD measurements.

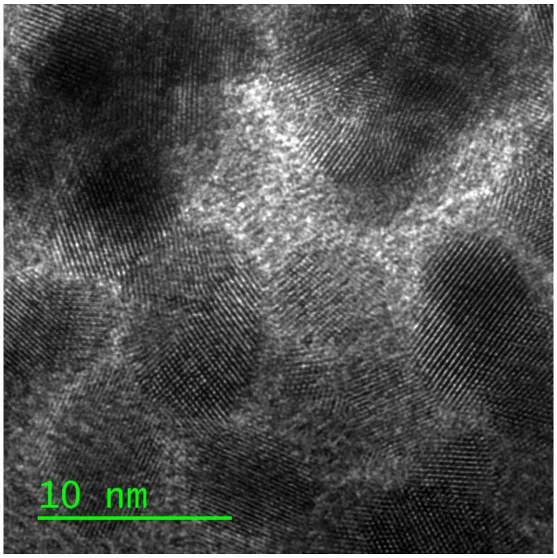

Fig. S17. HR-TEM image of Pt30/NCS85.

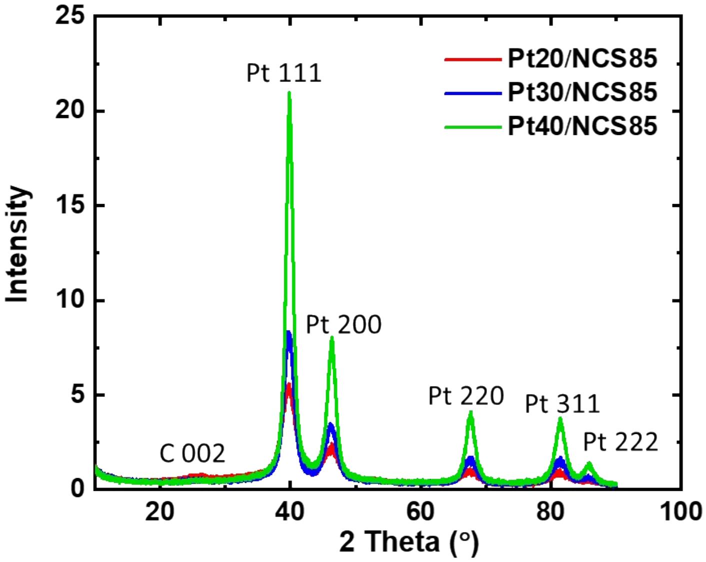

Fig. S18. XRD patterns of Ptx/NC85 films.

Table S5: Physical and electrochemical characteristics of Ptx/NCS85 catalyst layers in PEM fuel cell

Sample	No. of ALD cycles	Loading [mg/cm^2]^a	Particle size [nm]^b	ECSA [m^2/g$_{Pt}$]^c	Pt SA from TEM [m^2/g$_{Pt}$]^d	Pt surface Utilization [%]^e	Tafel slope [mV/dec]
Pt20/NCS85	20	0.26	3.5 ± 0.3	64.5	79.7	81	114.9
Pt30/NCS85	30	0.44	5.0 ± 0.7	43.0	56.4	76	91.8
Pt40/NCS85	40	0.60	6.4 ± 1.1	44.6	43.5	100	94.3

[a] Pt mass loading is measured using X-ray fluorescence (XRF,Spectro Xepos HE XRD Spectrometer).
[b] Particle size determined from TEM images in Figs 4a-c.
[c] Electrochemically active surface area (ECSA) obtained from anodic HUPD charges.
[d] Calculated by assuming that all Pt NPs are spherical in shape and using a Pt density of 21.45 g/cm^3.
[e] Utilization calculated by dividing ECSA from the HUPD charges by SAestimated from the Pt NP size seen by TEM

Table S6: Ptx/NCS85 catalyst layer characteristics and performance in fuel cell (at 0.9 V, 80 ℃, 100% RH, H_2/O_2)

Cathode Layer	Mass activity [A/mg$_{Pt}$]	Specific activity [mA/cm$^2_{Pt}$]
Pt20/NCS85	0.16	0.24
Pt30/NCS85	0.25	0.40
Pt40/NCS85	0.20	0.44
Pt/C GDE	0.10	0.27
Pt/C CCM	0.16	0.29

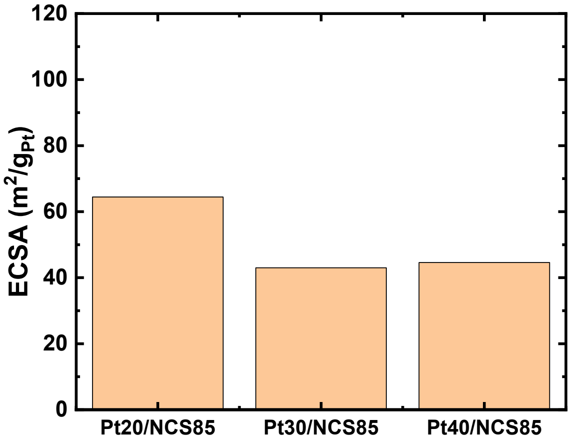

Fig. S19. Electrochemically active surface area (ECSA) determined from the charge passed during hydrogen desorption (HUPD peaks) for the Pt/NCS85 catalyst layers in the MEA.

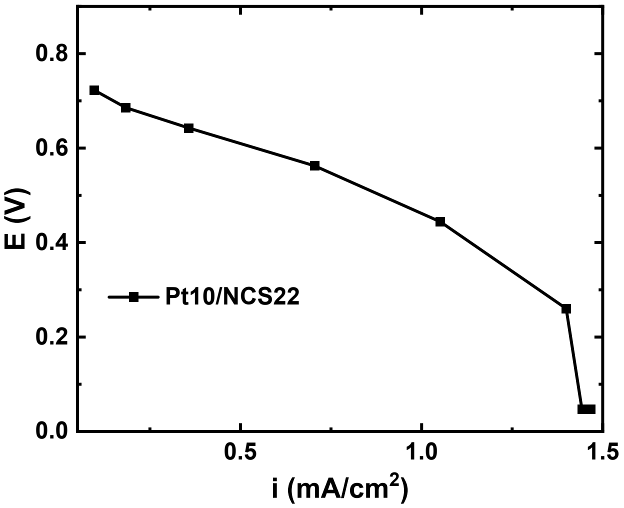

Fig. S20. IR-corrected H_2/Air performance plot for Nafion-infiltrated Pt10/NCS22 catalyst layer in an MEA at 80 ℃ and 150 kPa_{abs} back pressure.

References

1. Y. K. Sun, Z. Chen, H. J. Noh, D. J. Lee, H. G. Jung, Y. Ren, S. Wang, C. S. Yoon, S. T. Myung and K. Amine, *Nat. Mater.*, 2012, **11**, 942–947.

6. S. Korkut, J. D. Roy-Mayhew, D. M. Dabbs, D. L. Milius and I. A. Aksay, *ACS Nano*, 2011, **5**, 5214–5222.

7. S. Ohya; Y. Fujii, S. Yao, Y. Asano, K. Nakayama, K. Fukunaga, U.S. Patent No. 6,565,962.

8. V. Birss, X. Li, D. Banham, D. Y. Kwok. U.S. Patent No. 10,258,932.

17. K. Kimijima, A. Hayashi and I. Yagi, *Chem. Commun.*, 2008, **44**, 5809–5811.

48. X. Wang, Q. Zhu, S.M. Mahurin, C. Liang, S. Dai, *Carbon.* 2010, **48**, 557.

49. D. Feng, Y. Lv, Z. Wu, Y. Dou, L. Han, Z. Sun, Y. Xia, G. Zheng, D. Zhao, *J. Am. Chem. Soc.* 2011, **133**, 15148.

50. K. Nomura, H. Nishihara, N. Kobayashi, T. Asada, T. Kyotani, *Energy Environ. Sci.* 2019, **12**, 1549.

51. K. Kimijima, A. Hayashi, I. Yagi, 2009, *US 2009/0233792 A1.*

52. Z. Wang, F. Li, N.S. Ergang, A. Stein, *Chem. Mater.,* 2006, **18**, 5543.

53. M. Si, D. Feng, L. Qiu, D. Jia, A. A. Elzatahry, G. Zheng, D. Zhou, J. *Mater. Chem. A,* 2013, **1**, 13490.

54. E. P.Barrett, L. G. Joyner, P. P. Halenda, *J. Am. Chem. Soc.* 1951, **73**, 373.

55. X. Li, D. Banham, F. Feng, F. Forouzandeh, S. Ye, D. Kwok, V. Birss, *Carbon*, 2015, **87**, 44.

56. M. Thommes, K. Kaneko, A. V. Neimark, J. P. Oliver, F. Rodriguez-Reinoso, J. Rouquerol, K. S. W. Sing, *Pure Appl. Chem.,* 2015, **87**, 1051.

57. F. Forouzandeh, X. Li, D. W. Banham, F. Feng, A. J. Kakanat, S. Ye, V. Birss, *J. Power Sources,* 2018, **378**, 732.

58. K.P. Gierszal, M. Jaroniec, *J. Am. Chem. Soc.,* 2006, **128**, 10026.